Supporting Information

Intrinsic Carbon Nanotube Liquid Crystalline Elastomer Photoactuator for High-Definition Biomechanics

Juzhong Zhang,[†][a] Dandan Sun,[†][a] Bin Zhang,[a] Qingqing Sun,[a] Yang Zhang,[b] Shuiren Liu,[*][a] Yaming Wang,[c] Chuntai Liu,[c] Jinzhou Chen,[a] Jingbo Chen,[a] Yanlin Song,[d] Xuying Liu[*][a]

a. *School of Materials Science and Engineering, Henan Key Laboratory of Advanced Nylon Materials and Application, Henan Innovation Center for Functional Polymer Membrane Materials, Zhengzhou University, Zhengzhou, 450001, China. E-mail: lsrzzdx@zzu.edu.cn(S. Liu); liuxy@zzu.edu.cn(X. Liu).*
b. *Center of Advanced Analysis & Gene Sequencing, Zhengzhou University, Zhengzhou, 450001, China.*
c. *National Engineering Research Center for Advanced Polymer Processing Technology, Key Laboratory of Advanced Materials Processing & Mold, Ministry of Education, Zhengzhou University, Zhengzhou, 450001, China.*
d. *Key Laboratory of Green Printing, Institute of Chemistry, Chinese Academy of Sciences, Zhongguancun North First Street 2, Beijing, 100190, China.*

† These authors contribute equally to this work.

Corresponding authors: lsrzzdx@zzu.edu.cn(S. Liu); liuxy@zzu.edu.cn(X. Liu).

Experimental Procedures

*Materials:*1,4-bis-[4-(6-acryloyloxyhexyloxy)benzoyl-oxy]-2-methylbenzene (RM82, 95%), was purchased from HEOWNS. Pentaerythritol tetra(3-mercaptopropionate) (PETMP, 95%), 1,10-decanedithiol (DT, 96%), 2,2-dimethoxy-2-phenylacetophenone (DMAP), acryloyl chloride (AC, 96%), propionyl chloride (PC, 98%), anhydrous dichloromethane (H_2O < 0.004%), dipropylamine (DPA, 99%), and 10-undecenoyl chloride (UEC, 98%) were obtained from Aladdin. Hydroxylated multiwalled carbon nanotubes and multiwalled carbon nanotubes (MWNT-OH and MWNT, 95%, 0.2–2 μm height and 5–15 nm diameter, hydroxylation content 5.58 wt.%) were obtained by XFNANO Materials Tech. Triethylamine (99%) was supplied by Adamas-Beta. Undecanoyl chloride (UAC, 98%) was obtained from Macklin. All materials were used as received unless otherwise noted.

Synthesis and purification of f-MWNTs: To remove moisture, 200 mg MWNT-OH was dried in a vacuum at 60 °C for 12 h. MWNT-OH (200 mg, 0.656 mmol) was sonicated in 40 mL of anhydrous dichloromethane filled with nitrogen for 60 min to obtain a homogeneous suspension. Triethylamine (0.93 ml, 6.56 mmol) was slowly added dropwise to the suspension to neutralize acid at 0 °C under nitrogen. Then, acryloyl chloride (0.54 ml, 6.56 mmol) was slowly added dropwise to the mixture. The mixture was stirred at 0 °C under N_2 for 4 h and then at room temperature for 2 h. Next, the reaction mixture was centrifuged at 3000 rpm for 2 min to remove the solvent. To remove unreacted monomer (triethylamine hydrochloride, etc.) and recover solid black powders, the mixture was filtered through a 0.45 μm pore-size membrane and washed thoroughly with dichloromethane and ethanol. Finally, the black powders (MWNT-AC) were collected on the membrane and dried under vacuum at 80 °C for 24 h. The method to covalently graft MWNT-OH with propionyl chloride, 10-undecenoyl chloride, or undecanoyl chloride was the same as the above method. Hydroxylated MWNTs were functionalized (f-MWNTs) with propionyl chloride, 10-undecenoyl chloride, or undecanoyl chloride and labeled as MWNT-PC, MWNT-UEC, and MWNT-UAC, respectively.

Fabrication of Intrinsic LCE and f-MWNTs/LCE Nanocomposites: Non-bonded nanocomposites and the intrinsic covalent polymer with f-MWNTs were synthesized by a one-pot method. These monodomain LCEs were prepared using two-stage cross-linking coupled with uniaxial stretching. Specifically, RM82 (1 g, 1.46 mmol) and 5 wt.% DMPA (0.0698 g, 0.25 mmol) were dissolved in toluene, and the mixture was heated at 80 °C to form a homogeneous solution. DMPA served as the photoinitiator for photopolymerization during uniaxial stretching. PETMP (0.0872 g, 0.1606 mmol), DT (0.3107 g, 1.4454 mmol), and f-MWNTs (0.0013 g, 0.1 wt.%) were added to the solution, and then 1% DPA in toluene (0.20784 g, 0.02054 mmol) was added as the Michael addition reaction catalyst. The mixed solution was shaken on a vortex mixer (SCILOGEX MX-S) for 1 h to ensure the formation of a homogeneous dispersion, which was then cast into a polytetrafluoroethylene (PTFE) mold and heated at 60 °C for 12 h to accomplish thiol-acrylate Michael addition. It was then kept under vacuum at 80 °C for 24 h to evaporate toluene and remove bubbles. When cooled to room temperature, the samples were uniaxially stretched and placed under 365 nm UV light for 15 min to complete the acrylate-acrylate crosslinking reaction to transform it from a polydomain state to a monodomain state.

Fabrication of Multi-stimuli-Responsive Actuators: The monodomain LCE-based samples were cut into 9 mm long and 5 mm wide sheets along the stretching direction. An actuator was fabricated by layer-by-layer stacking using the mixed monomer solution as the adhesive, followed by thermal polymerization for 6 h.

Fabrication of light-driven artificial flower: The light-driven artificial flower was assembled by a petal-shaped intrinsic CNTs/LCE sheet and a 3D-printed pedestal. The pedestal is prepared by a 3D printer (A150-2, Shenzhen Liantao E-commerce Co., Ltd.) using PLA. And the intrinsic CNTs/LCE sheet was cut into petal shapes through kirigami. Then the petals were fixed on a 3D-printed pedestal, and manually unfolded the petals and permanently fixed the shape by UV polymerization.

Fabrication of snake-like crawling actuator: The snake-like crawling actuator was prepared from a polydomain intrinsic CNTs/LCE sheet, which was stretched and bended around four tubes to form a snake shape. Then the snake-like sample was polymerized with 365 nm UV light to obtain the permanent shape.

Fabrication of bionic hand: The bionic hand is realized by modifying the commercially available robotic hand (Hiwonder Co. Ltd). The original controller and power source are first removed. Then the monodomain intrinsic CNTs/LCEs were cut into strips (the major axis of strips is along the director). One edge of the strip was connected to the finger bone, drive shaft and the other edge was fixed to the palm.

Characterization: All LCE samples were characterized using the attenuated total reflection mode of the Fourier-transform infrared spectrometer (Bruker, Tensor-27). Differential scanning calorimetry measurements were conducted on a TA DSC25 at 10 °C min^{-1} with a mechanical temperature controller. The examination used the up-down-up mode, and the first heating was used to remove the thermal history, while the first cooling and the second heating were used for analysis. Optical and POM images were obtained using polarized microscopy (Leica, DM2700M) equipped with a cold and hot stage (Linkam, THMS600). 2D-Wide-angle X-ray diffraction (Bruker, D8 Discover) was performed to explore the transformation of liquid crystal-isotropic phases during the heating

and cooling process and changes in the order parameter *S* during phase transitions. The light source was a Cu target, λ = 0.154 nm, the spot diameter was 1 mm, the distance between the sample and the detector was 85 mm, and the diffraction angle 2θ scanning range was 5–35°. Scanning electron microscopy (Zeiss, Auriga-Bu), spherical aberration-corrected transmission electron microscopy (JEM ARM300F), and atomic force microscopy (Bruker, Nano IR 3) were used to examine the morphology of samples and compatibility between MWNT-F and LCE matrix. The fracture surface samples were prepared by tension, while the cross-section samples were prepared by cooling (-80 °C) in a cryomicrotome system and slicer (Leica, EM UC7 FC7). All fracture and cross-section samples with a thickness of 1 μm were coated with a gold film using a vacuum coating instrument (Leica, EM ACE600). Spherical aberration-corrected transmission electron microscopy was performed on ultramicrotomed samples with a thickness of 50 nm, operated at an accelerating voltage of 300 kV. The ultraviolet-visible-near infrared spectra of materials and LCE samples were obtained using a UV-VIS-NIR spectrophotometer (Agilent, Cary 5000). The absorption of all samples was measured from 200–1200 nm by using a UV-VIS-NIR spectrophotometer.

Mechanical Tests: The tensile properties of all LCE samples were characterized using a universal tensile testing machine (SUNS, UTM5202) with a stretching speed of 5 mm min^{-1} with a 50 N sensor at room temperature.

Actuation Stress Tests: The samples were fixed on the universal stretching machine, where the displacement was controlled at 1 mm min^{-1}, and the force was controlled at 0.01 N. The ultraviolet laser and infrared laser (with different power densities) were used to alternately switch and irradiate the samples to explore the relationship between the light power density and actuation stress. At the same time, an infrared thermal imager (FLIR, E60) was used to measure the relationship between the temperature and light power density. The NIR and UV actuation of the LCE samples were measured under an 808 nm NIR laser (LASEVER, LSR808H-8W-FC) and a 355 nm UV laser (LASEVER, LSR355CP-1W-FC).

Gel Content Tests: Samples were dried for 12 h and extracted with chloroform in a soxhlet extractor for 24 h at 85 °C in an oil bath. The sample was dried under vacuum at 80 °C for 24 h to remove the absorbed solvent. We used the following formula to calculate:

$$\text{Gel content} = \frac{m_1}{m_2} \times 100\%$$

where m_1 and m_2 are the masses of the dried sample after and before extraction, respectively.
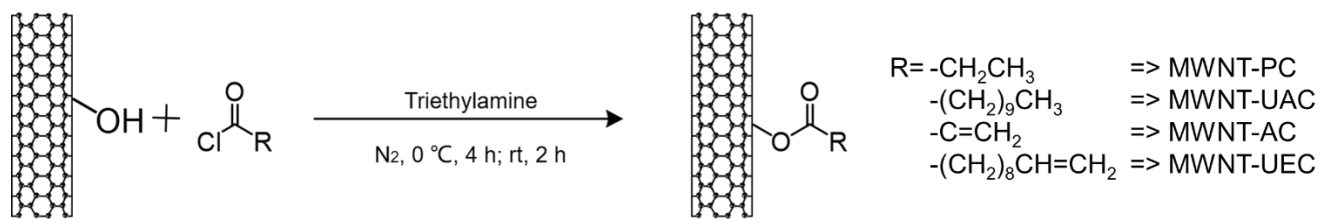
Fig. S1. The synthesis principle of f-MWNTs.

R= -CH$_2$CH$_3$ => MWNT-PC
-(CH$_2$)$_9$CH$_3$ => MWNT-UAC
-C=CH$_2$ => MWNT-AC
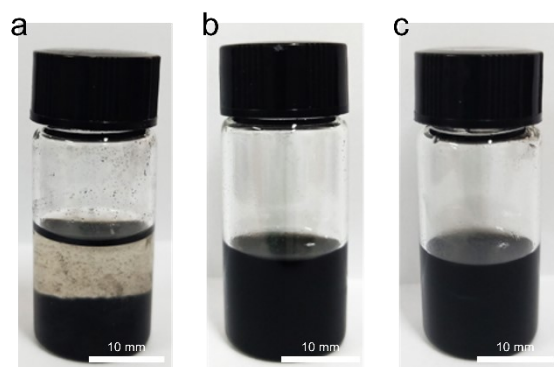-(CH$_2$)$_8$CH=CH$_2$ => MWNT-UEC

Fig. S2. (a-c) Photographs of the MWCNT/LCE solutions after being placed at room temperature for 12 h. The MWNT-OH/LCE (a) solution settled first, while MWNT-AC/LCE (b) and MWNT-UEC/LCE (c) solutions remained dispersed.
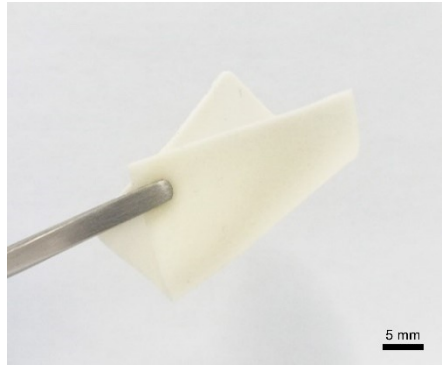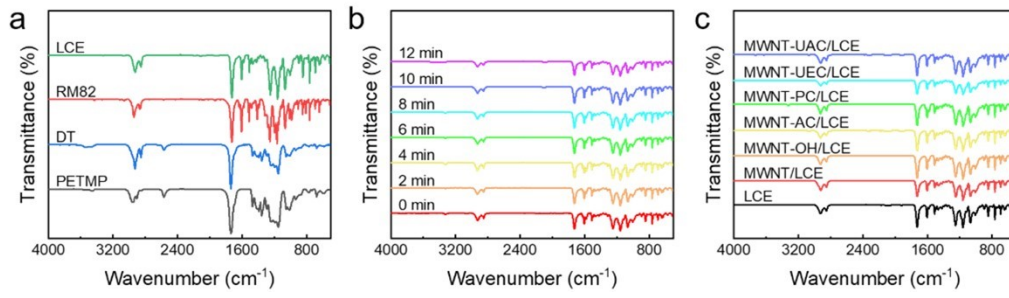
Fig. S3. The photograph of LCEs showing good flexibility.

Fig. S4. FTIR spectra of (a) raw materials and (b) different photopolymerization times of the LCEs. (c) FTIR spectra of intrinsic LCE and MWNT-F/LCE nanocomposites.
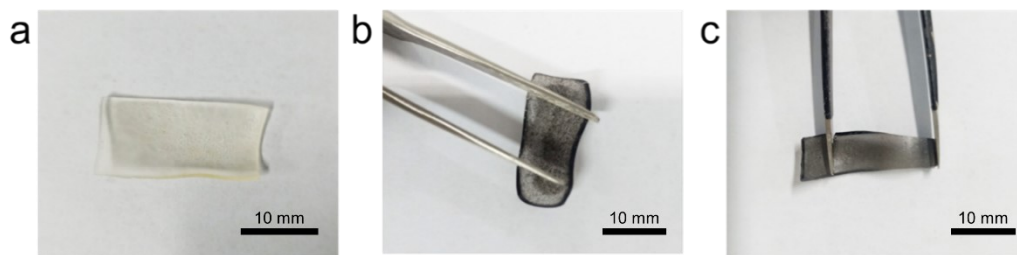
Fig. S5. Intrinsic LCE and MWNT-F/LCE nanocomposites swelled in chloroform: (a) LCE; (b)MWNT-OH/LCE; (c)MWNT-AC/LCE. There are many aggregated carbon nanotubes in MWNT-OH/LCE, while MWNT-AC/LCE was relatively uniform, indicating that covalent grafting improved the dispersion of MWNT-AC.
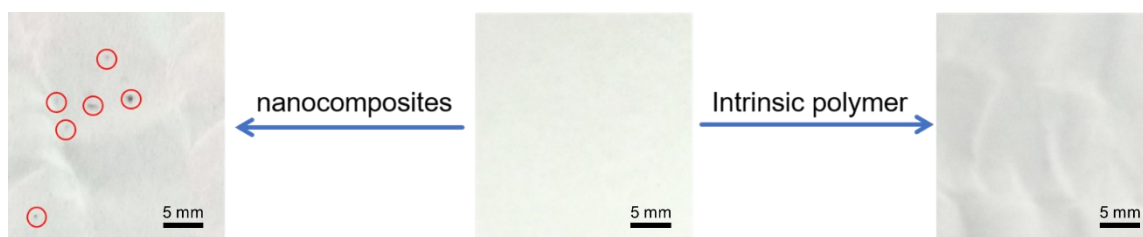
Fig. S6. Filter paper used to extract MWNT-F/LCE nanocomposites and intrinsic LCE. After chloroform extraction, there was no trace of the intrinsic LCE on the filter paper, while traces of carbon nanotubes and the LCE matrix appeared on the filter paper in the non-bonded nanocomposites.
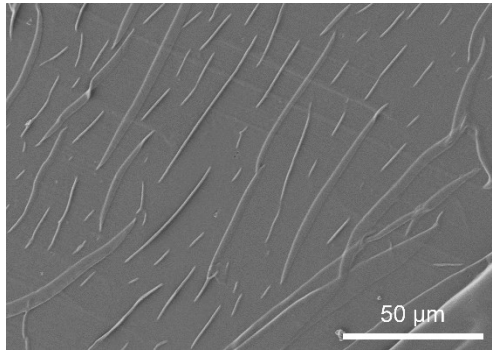
Fig. S7. SEM images showing the morphology of the MWNT-AC/LCE. The sample was prepared from frozen sections
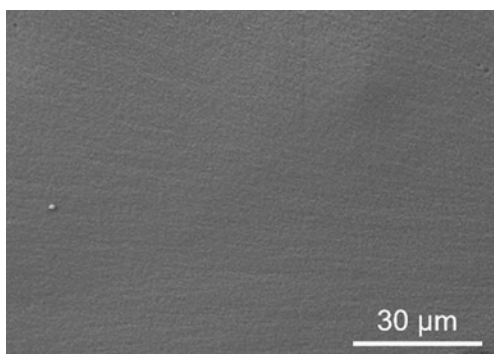
Fig. S8. SEM images showing the morphology of the LCE tensile fracture surface.
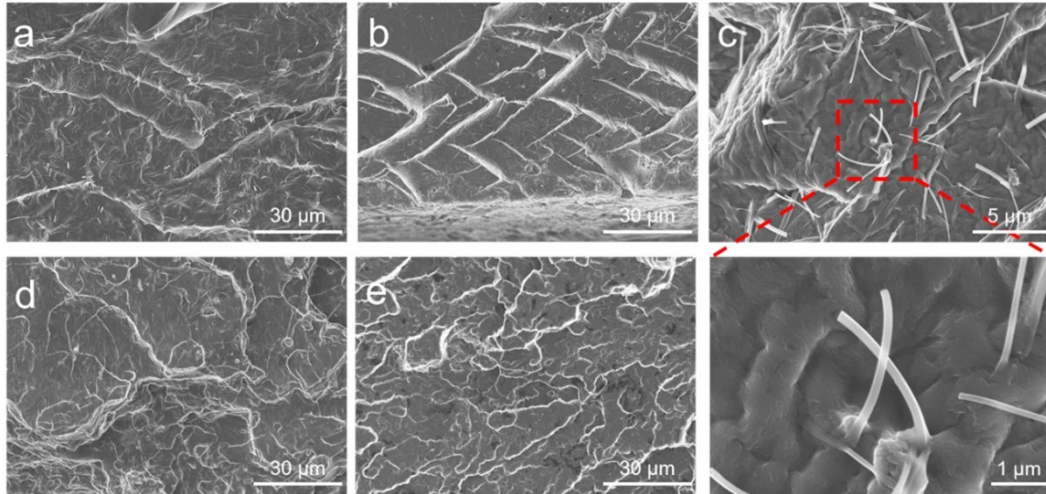
Fig. S9. SEM images showing the morphology of the tensile fracture surface: (a) MWNT-AC/LCE, (b) MWNT-UEC/LCE, and (c) an enlarged view of a section. SEM images showing the morphology of sections freeze-quenched in liquid nitrogen: (d) MWNT-AC/LCE and (e) MWNT-UEC/LCE.
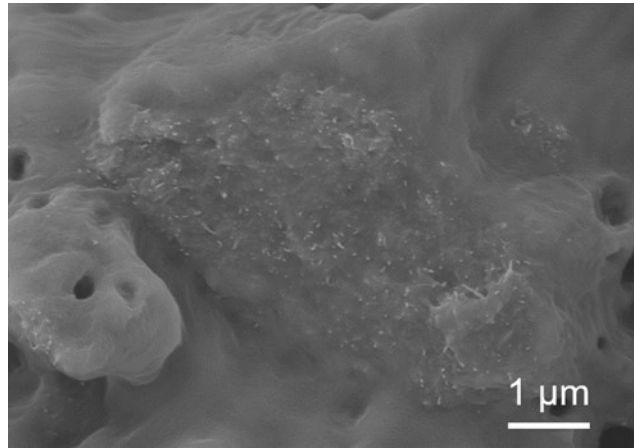
Fig. S10. SEM image showing the morphology of the MWNT-OH/LCE tensile fracture surface, which shows the poor compatibility of the carbon nanotubes with matrix and their agglomeration.
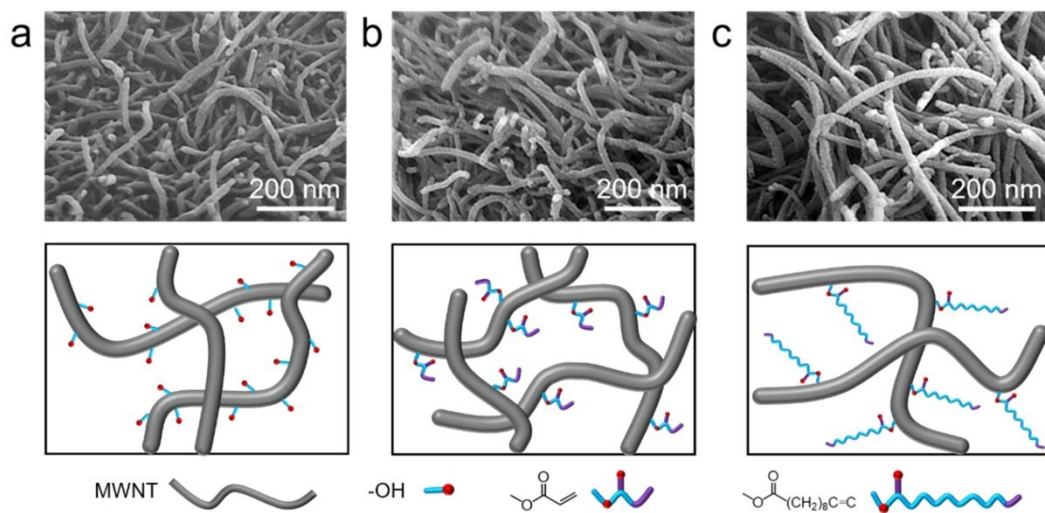
Fig. S11. The morphology of MWNT-OH before and after modification: (a) MWNT-OH; (b) MWNT-AC; (c)MWNT-UEC. The diameter of MWNT-OH increased after modification.
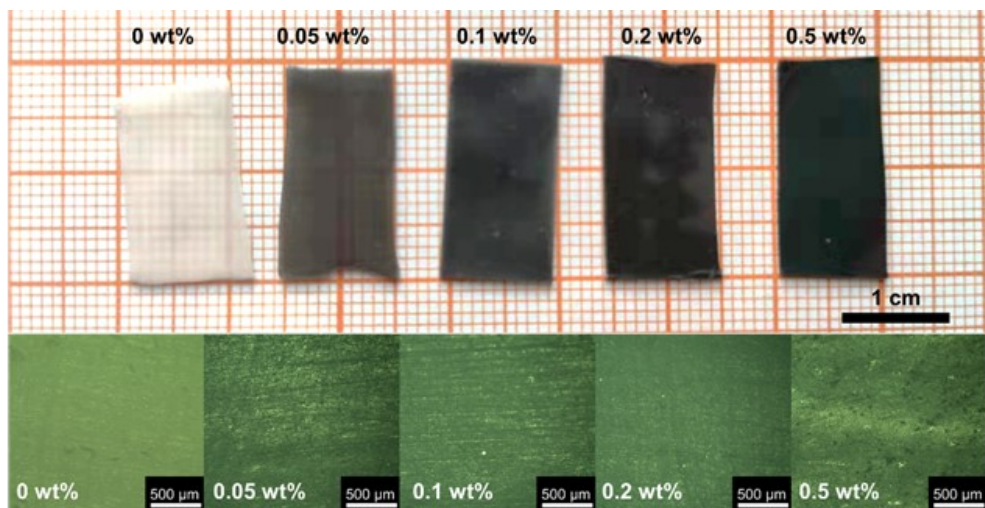
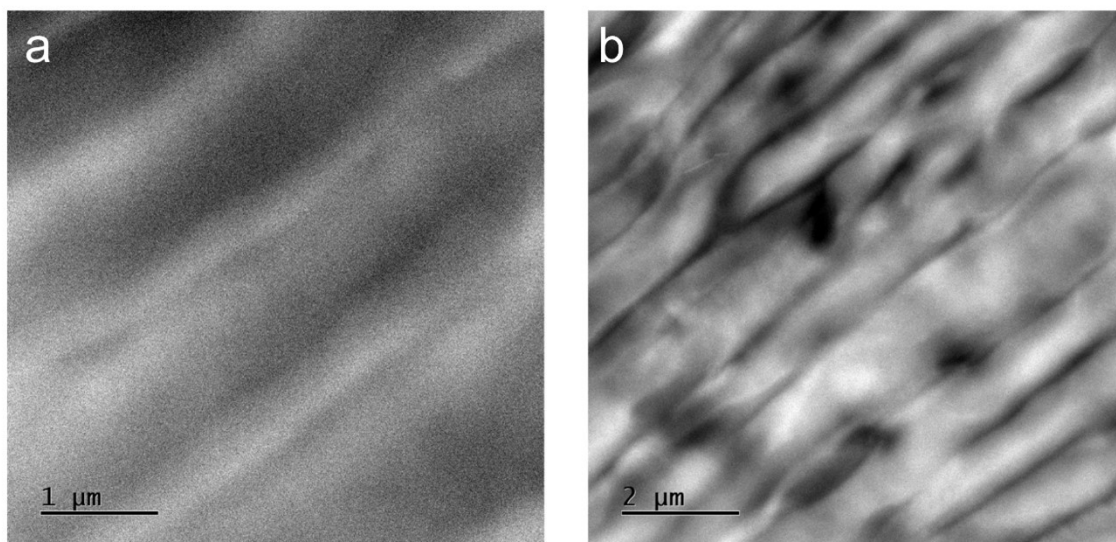**Fig. S12.** Optical photos of intrinsic CNTs/LCE materials with different contents of functionalized carbon nanotubes (MWNT-AC).

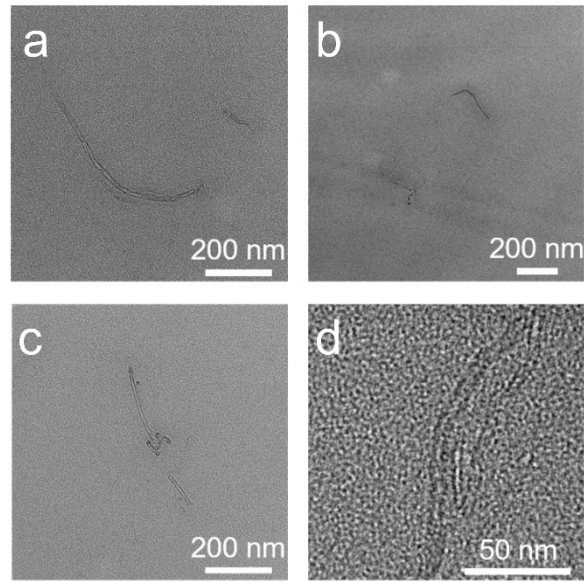**Fig. S13.** (a-b) TEM image of multiple well-oriented strip structures formed in MWNT-AC/LCE.

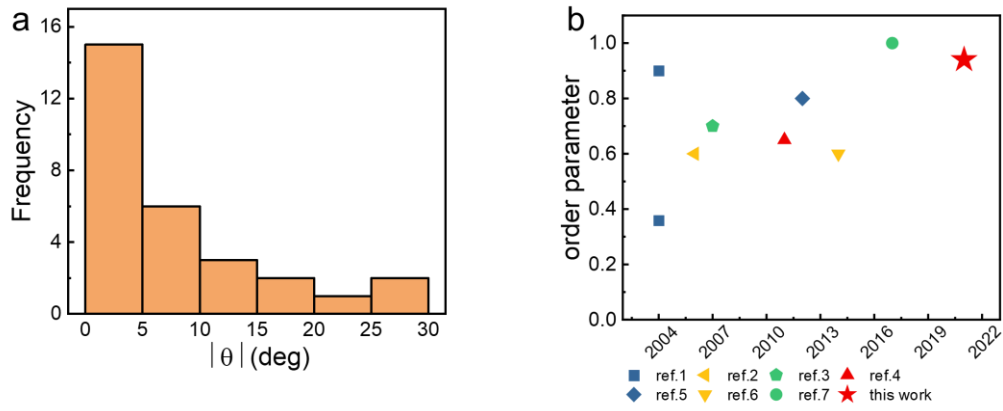**Fig. S14.** (a-d) The distribution of MWNT-AC at different regions in the MWNT-AC/LCE matrix.

Fig. S15. (a) Uniaxial stretching to orient the MWNT-AC, where the strip structure was preferentially aligned along the orientation direction. The number of different angles between the strip structure and the director. (b) A comparative summary of the carbon nanotubes' order parameter reported in similar literatures[1–7] on liquid crystals and carbon nanotubes and this work.
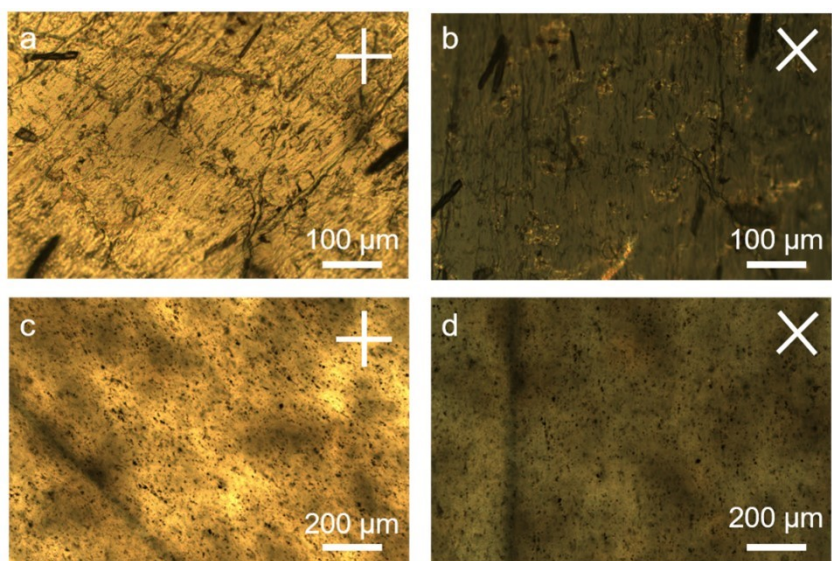
Fig. S16. (a) Optical image of the LCE under polarized light; (b) LCE rotated 45° under polarized light; (c) Optical image of MWNT-AC/LCE under polarized light; (d) MWNT-AC/LCE rotated 45° under polarized light
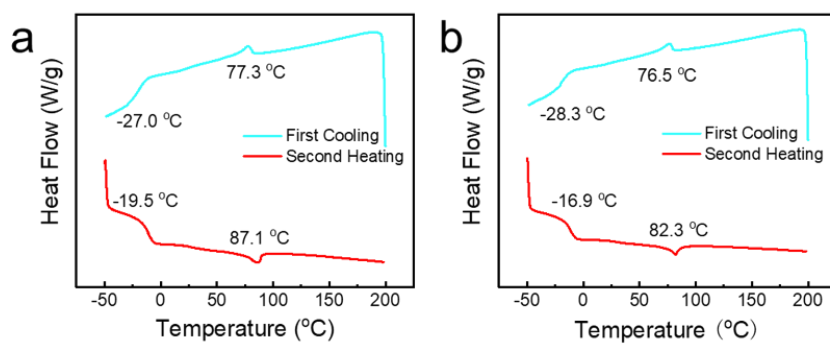
Fig. S17. DSC curves of (a) MWNT-PC/LCE; (b) MWNT-UAC/LCE during the first cooling scan (blue lines) and the second heating scan (red lines) at a rate of 10 °C min^{-1} under a nitrogen atmosphere.
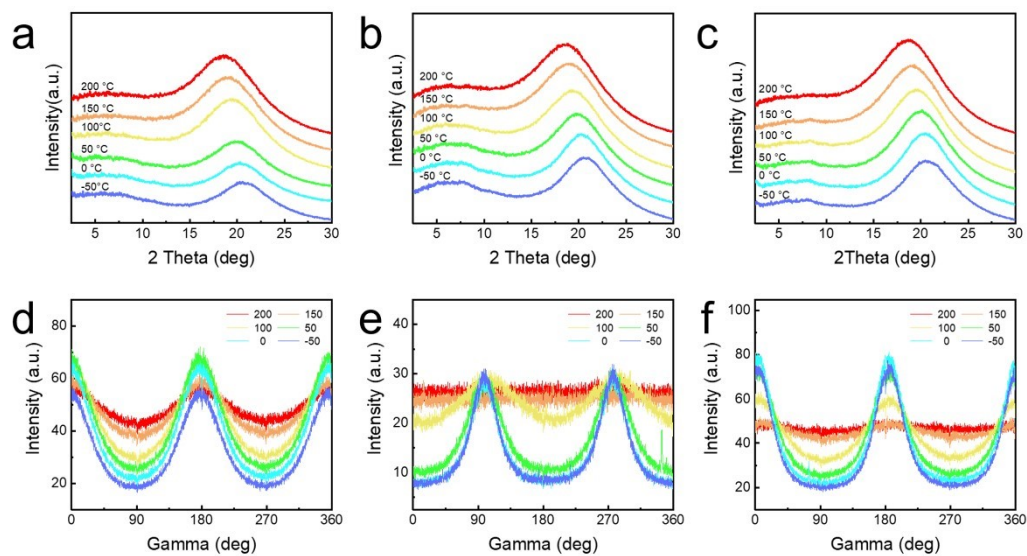
Fig. S18. 1D-WAXD patterns of (a) LCE, (b) MWNT-AC/LCE, (c) MWNT-UEC/LCE when heated from -50 °C to 200 °C. The heating rate was 10 °C min^{-1}, with a point taken every 50 °C. A plot of the intensity as a function of the azimuthal angle for (d) LCE, € MWNT-AC/LCE, and (f) MWNT-UEC/LCE during heating. The orientation degree of all samples decreased upon increasing the temperature.
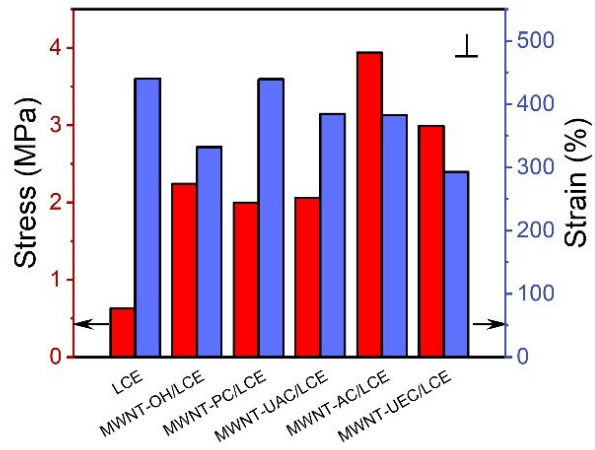
Fig. S19. The tensile strength and tensile strain of the intrinsic LCE and MWNT-F/LCE nanocomposites in the direction perpendicular to the director.
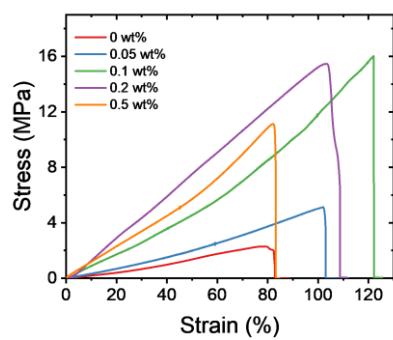
Fig. S20. Stress-strain curves of intrinsic CNTs/LCE materials (parallel to the stretching direction) with different contents of functionalized carbon nanotubes (MWNT-AC).
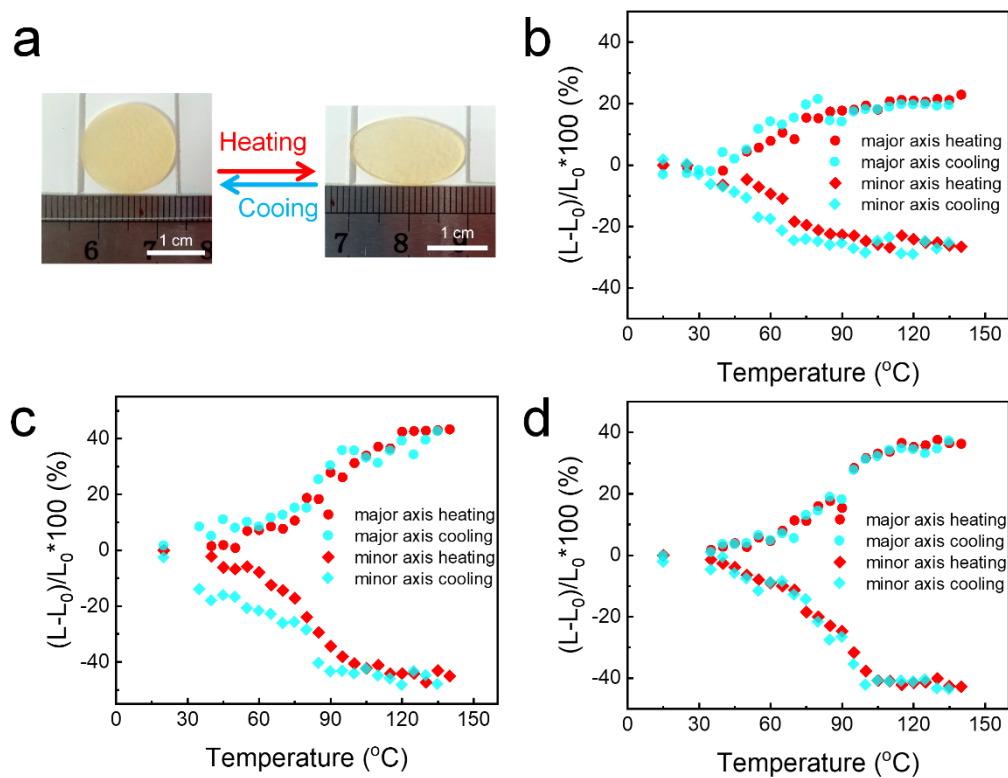
Fig. S21. (a) Shape-morphing behavior of LCE during cooling and heating. Its temperature was controlled by a hot stage, the length changes of the long axis and short axis were measured every 5 °C, and the deformation rate was calculated. The temperature dependence of the deformation rate of the major axis and minor axis of the ellipse: (b) LCE stretched by 150%; (c) LCE stretched by 200%; (d) MWNT-UEC/LCE stretched by 200%.
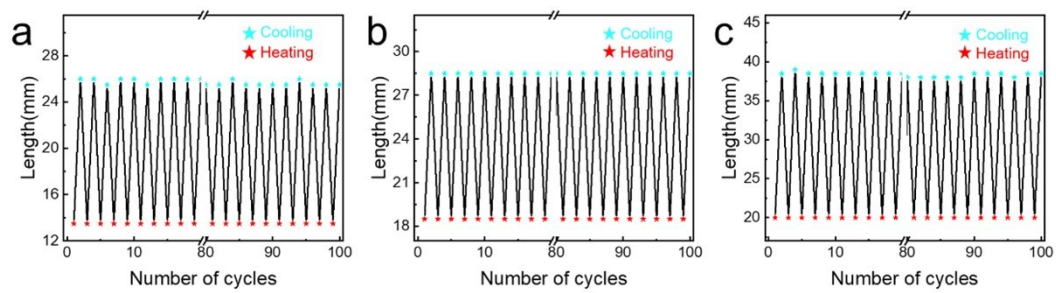
Fig. S22. Stability of the LCEs during cooling (20 °C) and heating (180 °C) cycles : (a) LCE, (b) MWNT-AC/LCE, and (c) MWNT-UEC/LCE.
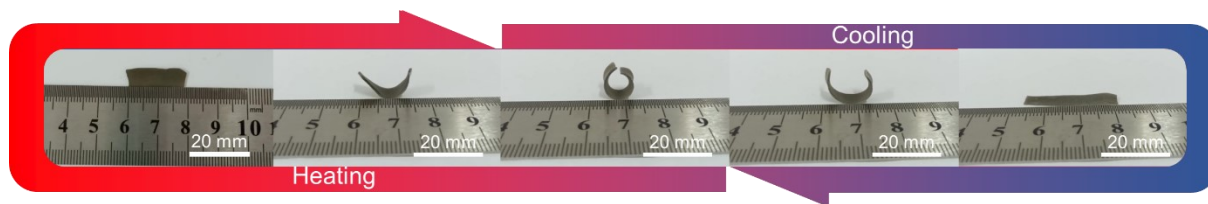
Fig. S23. Intrinsic MWNT-AC/LCE strip exhibited a two-stage reversible deformation during cooling and heating process (curling and unfolding at about 100 °C). The bending deformation shown in Figure S23 is realized by local heating of the sample with a thermal gun. During the heating and cooling process, the temperature of the sample is uneven, which makes the deformation of it inconsistent, resulting in bending behavior.
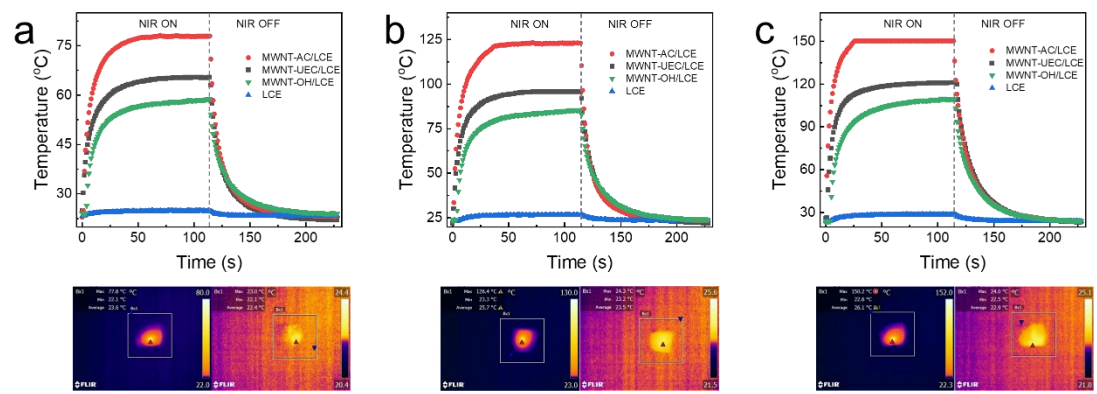
Fig. S24. Diagram and corresponding infrared images showing the temperature dependency of LCE and M-AC/LCE on the NIR laser irradiation power density: (a) 318 mW cm^{-2}, (b) 604 mW cm^{-2}, and (c) 870 mW cm^{-2}.
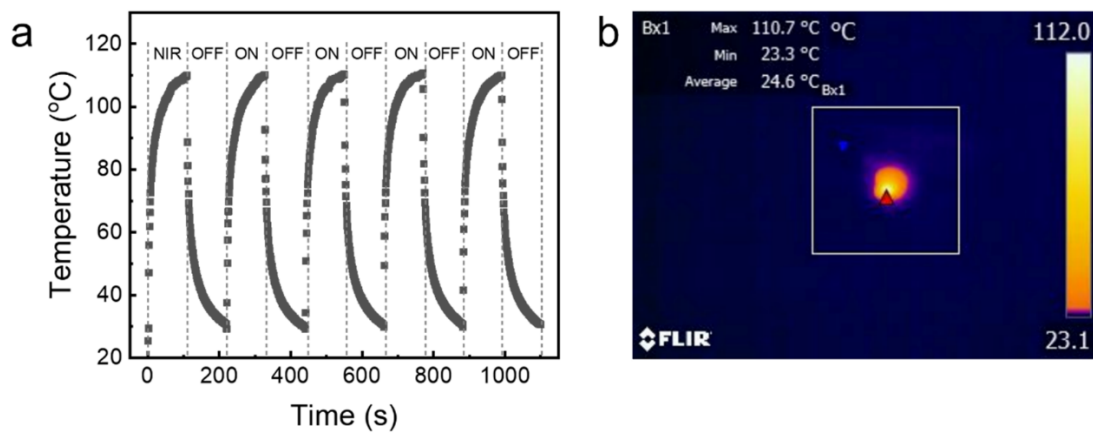
Fig. S25. (a) The relationship between multilayer MWNT-AC/LCE actuator surface temperature and laser irradiation time. When the actuator was irradiated by an infrared laser with a power density of 604 mW cm^{-2}, it reached the highest temperature in about 6 s. After turning off the laser, the temperature of the actuator surface returned to its original values. (b) Infrared image of the MWNT-AC/LCE actuator at its maximum temperature.
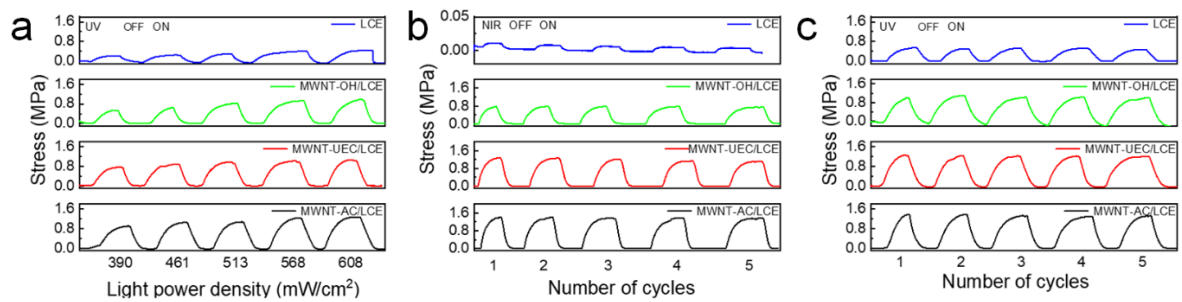
Fig. S26. (a) UV laser light power density vs. actuator stress curves of LCE. The actuation stability of the LCE under an infrared laser density of 344 mW cm^{-2} (b) and ultraviolet light density of 568 mW cm^{-2} (c).
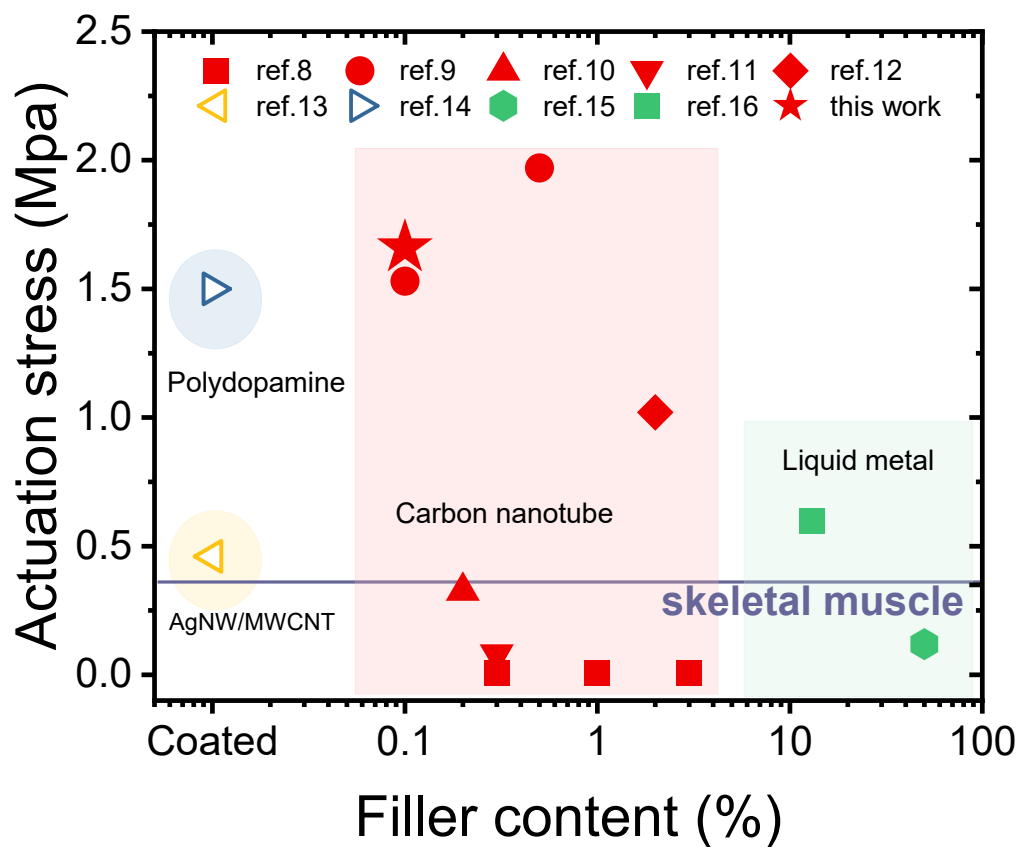
Fig. S27. A comparative summary of the maximum actuation stress reported in similar works.[8–16]

Fig. S28. Time vs. actuating stress curves of LCE samples with different contents of MWNT-AC by a NIR laser with a power density of 344 mW cm^{-2} and wavelength of 808 nm.
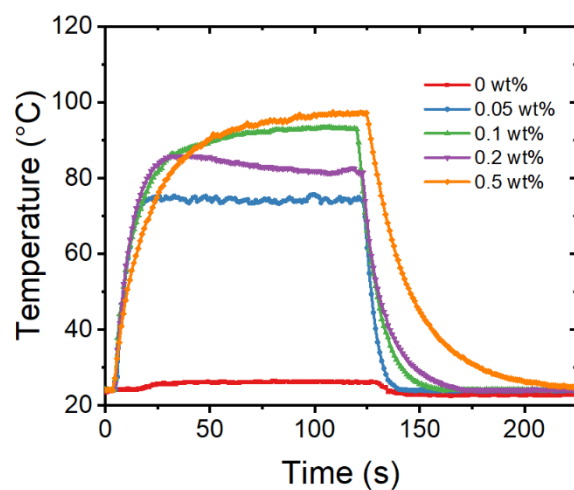
Fig. S29. The temperature changes of intrinsic CNTs/LCE materials with different contents of MWNT-AC under irradiation by a NIR laser with a power density of 344 mW cm^{-2} and wavelength of 808 nm.

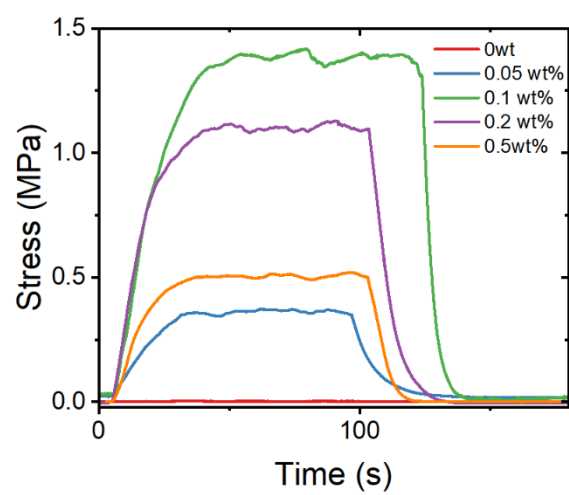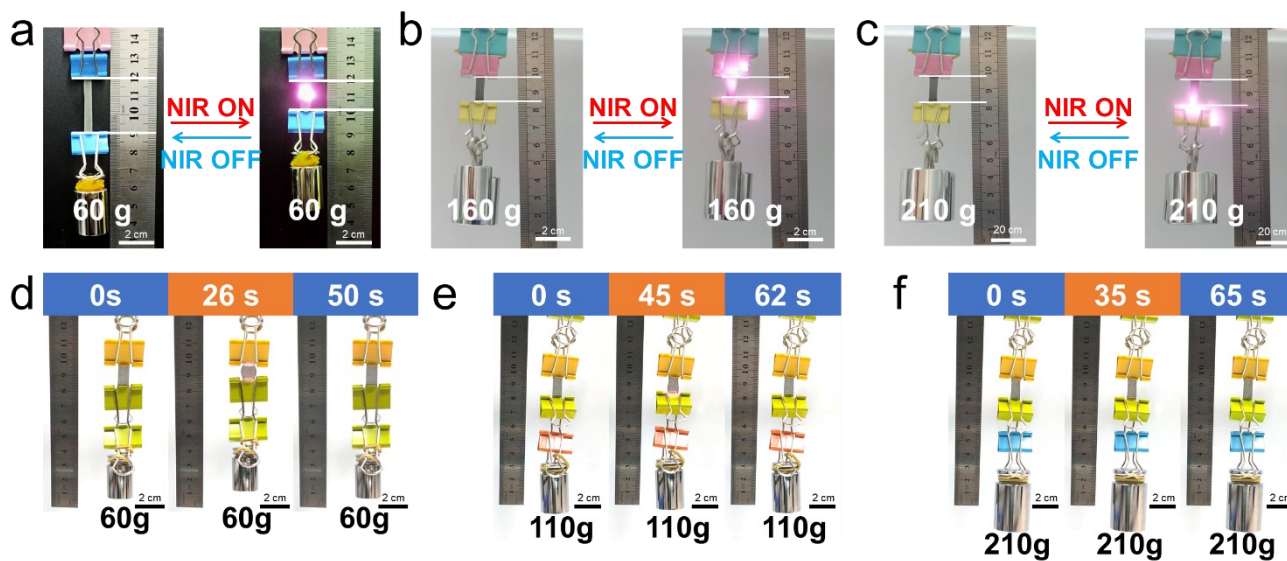**Fig. S30.** (a)The image of the MWNT-AC/LCE (ca. 53 mg) lifting a load over 1000 times heavier than itself. It exhibited reversible recovery under NIR light. And photos of MWNT-AC/LCE (ca. 36 mg) lifting a 160.67 g (b) and a 210.67 g (c) load after irradiation by the infrared laser alternate switch. (d-f) snapshots of the MWNT-AC/LCE (ca. 33.5 mg) lifting loads (60g, 110g, and 210g).

33
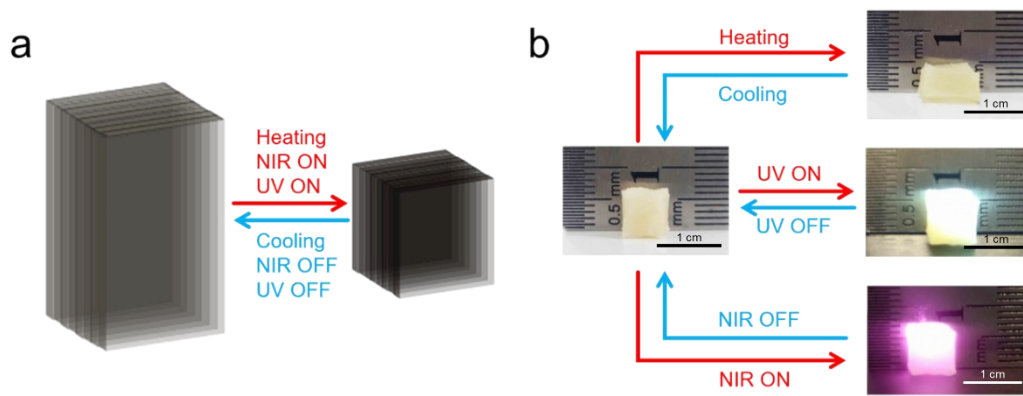
Fig. S31. (a) Schematic of the intrinsic LCE actuator. (b) Photos of the multilayer LCE actuator exhibiting reversible contraction/stretching during heating and cooling, while showing a relatively weak response to infrared and ultraviolet lasers. (The processing time is 5 min)
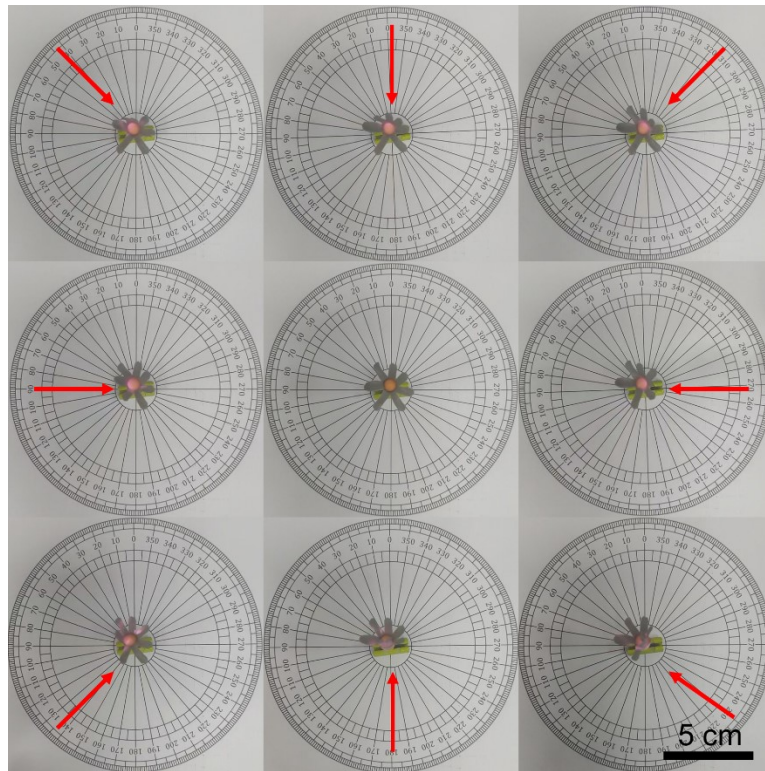
Fig. S32. Top-view snapshots of the artificial flower selectively closing with the NIR light (808nm, 344 mW cm^{-2}). The red arrow shows the direction of the light.

Table S1. Structure of different CNTs/LCE samples

Abbreviations	Dimension of CNTs	Modifier	Functional group	CNT concentration
MWNT-PC/LCE		Propionyl chloride	Propionate	0.1wt%
MWNT-UAC/LCE		Undecanoyl chloride	Undecanoate	0.1wt%
MWNT-AC/LCE	0.2–2 μm height and 5–	Acryloyl chloride	Acrylate	0.1wt%
MWNT-UEC/LCE	15 nm diameter	10-undecenoyl chloride	Undecenoate	0.1wt%
MWNT-OH/LCE		None	Hydroxyl	0.1wt%
MWNT/LCE		None	None	0.1wt%

Table S2. Gel content of intrinsic LCE and MWNT-F/LCE nanocomposites.

Samples	Quality before extraction m_1 (g)	Quality after extraction m_2 (g)	Gel content (%)
LCE	0.6975	0.6013	86.2
MWNT/LCE	0.6405	0.5481	85.6
MWNT-OH/LCE	0.3978	0.3766	94.6
MWNT-PC/LCE	0.7771	0.6882	88.6
MWNT-UAC/LCE	0.4850	0.4533	93.4
MWNT-AC/LCE	0.4878	0.4398	90.1
MWNT-UEC/LCE	0.5225	0.4723	90.4

Table S3. Tensile modulus and toughness data of different liquid crystal elastomers with different f-MWNTs

Materials	Parallel to the director		Perpendicular to the director	
	Tensile modulus (MPa)	Toughness (MJ m^{-3})	Tensile modulus (MPa)	Toughness (MJ m^{-3})
LCE	1.44±0.45	0.96±0.09	0.58±0.12	0.57±0.09
MWNT/LCE	7.25±1.41	2.26±0.91	4.25±0.89	4.27±0.87
MWNT-OH/LCE	5.32±1.38	2.47±0.76	3.06±0.87	3.40±1.09
MWNT-PC/LCE	2.76±0.86	1.80±0.60	3.05±0.58	2.78±0.63
MWNT-UAC/LCE	5.04±1.01	2.06±0.43	3.62±1.07	2.68±0.73
MWNT-AC/LCE	4.58±1.01	4.54±1.48	4.11±1.20	3.51±1.49
MWNT-UEC/LCE	4.33±2.13	4.62±1.35	3.14±1.10	2.51±0.71

Video S1. Video of the MWNT-AC/LCE lifting loads.

Video S2. The light response of the artificial flower at 3x speed.

Video S3. The snake-like crawling movements of a serpentine actuator controlled by NIR laser.

Video S4. The high-definition contral of the biomimetic prosthetic hand by NIR laser at 5x speed.

References

1   I. Dierking, G. Scalia and P. Morales, *J. Appl. Phys.*, 2005, **97**, 044309.
2   J. Lagerwall, G. Scalia, M. Haluska, U. Dettlaff-Weglikowska, S. Roth and F. Giesselmann, *Adv. Mater.*, 2007, **19**, 359-+.
3   G. Scalia, C. von Bühler, C. Hägele, S. Roth, F. Giesselmann and J. P. F. Lagerwall, *Soft Matter*, 2008, **4**, 570.
4   N. Puech, C. Blanc, E. Grelet, C. Zamora-Ledezma, M. Maugey, C. Zakri, E. Anglaret and P. Poulin, *J. Phys. Chem. C*, 2011, **115**, 3272–3278.
5   C. Zamora-Ledezma, C. Blanc and E. Anglaret, *J. Phys. Chem. C*, 2012, **116**, 13760–13766.
6   S. Azoz, A. L. Exarhos, A. Marquez, L. M. Gilbertson, S. Nejati, J. J. Cha, J. B. Zimmerman, J. M. Kikkawa and L. D. Pfefferle, *Langmuir*, 2015, **31**, 1155–1163.
7   N. Komatsu, W. Gao, P. Chen, C. Guo, A. Babakhani and J. Kono, *Adv. Funct. Mater.*, 2017, **27**, 1606022.
8   Y. Ji, Y. Y. Huang, R. Rungsawang and E. M. Terentjev, *Adv. Mater.*, 2010, **22**, 3436–3440.
9   H. Kim, J. A. Lee, C. P. Ambulo, H. B. Lee, S. H. Kim, V. V. Naik, C. S. Haines, A. E. Aliev, R. Ovalle-Robles, R. H. Baughman and T. H. Ware, *Adv. Funct. Mater.*, 2019, **29**, 1905063.
10 T. Guin, H. E. Hinton, E. Burgeson, C. C. Bowland, L. T. Kearney, Y. Li, I. Ivanov, N. A. Nguyen and A. K. Naskar, *Adv. Intell. Syst.*, 2020, **2**, 2000022.
11 C. Li, Y. Liu, C. Lo and H. Jiang, *Soft Matter*, 2011, **7**, 7511.
12 J. Liu, Y. Gao, H. Wang, R. Poling-Skutvik, C. O. Osuji and S. Yang, *Adv. Intell. Syst.*, 2020, **2**, 1900163.
13 H. Liu, H. Tian, J. Shao, Z. Wang, X. Li, C. Wang and X. Chen, *ACS Appl. Mater. Interfaces*, 2020, **12**, 56338–56349.
14 H. Tian, Z. Wang, Y. Chen, J. Shao, T. Gao and S. Cai, *ACS Appl. Mater. Interfaces*, 2018, **10**, 8307–8316.
15 M. J. Ford, C. P. Ambulo, T. A. Kent, E. J. Markvicka, C. Pan, J. Malen, T. H. Ware and C. Majidi, *Proc. Natl. Acad. Sci.*, 2019, **116**, 21438–21444.
16 J. Sun, Y. Wang, W. Liao and Z. Yang, *Small*, 2021, 2103700.